Edge-Delocalized Electron Effect on Self-Expediating Desolvation Kinetics for Low-Temperature Li—S Batteries

Yongzheng Zhang, Xiang Li, Yanli Wang,* Jianghao Zhu, Yinze Zuo,* Xiaomin Cheng, Tao Rong, Jing Zhang, Yang Hu, Hongzhen Lin, Jian Wang,* Liang Zhan,* and Licheng Ling

Lithium-sulfur (Li—S) batteries suffer from significant capacity degradation, which is limited by high barriers from interfacial desolvation, Li^+ transportation to sulfur redox conversions, exhibiting the depressive kinetics. Herein, the electron effect in the edge of catalysts is modulated and the corresponding strategy of self-transform Schottky heterojunction on MXene is proposed to achieve the edge delocalized electronic density. As a protocol, the electron-delocalized Schottky heterojunction of boron-doped MXene/TiO_2 (SH-MTB) is fabricated as electrochemical kinetic accelerators to realize fast Li^+ desolvation to promote rapid sulfur conversion kinetics under low-temperature. Specifically, the Schottky heterojunction with edge effect expedites the dissociation kinetics of $[Li(solvents)_x]^+$ to generate free Li ions, as well-confirmed by theoretical calculations and ex-situ/in situ electrochemical characterizations. Encouragingly, higher practical areal capacity (5.0 mAh cm^{-2}) and negligible self-discharge behaviors are achieved under low-temperature environments. A large areal pouch cell with 200 mg$_s$ exhibits 9.3 mAh cm^{-2} under a lean electrolyte amount (5 µL mg^{-1}), much better than state-of-art reports. As further indicated by electronic microscopies, spectroscopical measurements and X-ray tests, the SH-MTB stabilizes the chemical structure during charge/discharge process, showing promising potential of Schottky heterostructure toward accelerating the cascade carrier kinetics in Li metal battery under low-temperature.

1. Introduction

The ever-growing lithium-sulfur (Li—S) batteries with abundant sulfur reserves offer a theoretical energy density over 2600 Wh kg^{-1}, demonstrating great application perspective.[1–4] However, some critical interfacial kinetic obstacles, including the sluggish Li^+ desolvation process, unfavorable sulfur redox kinetics of polysulfide conversion and Li_2S delithiation, cause significant capacity attenuation or even failure.[5–8] As illustrated in **Figure 1a**, decreasing environmental temperature to lower temperature, the above-mentioned kinetics of desolvation, diffusion and delithiation reaction would be retarded, especially under high-mass-loading cells. Among them, the $Li(solvents)_x^+$ desolvation behaviors at the electrode/electrolyte interface is more sensitive to the influence of temperature, exhibiting much higher barrier and the rate-determining step for successive sulfur redox reactions.[9–12]

Y. Zhang, X. Li, Y. Wang, J. Zhu, T. Rong, L. Zhan, L. Ling
State Key Laboratory of Green Chemical Engineering and Industrial Catalysis
State Key Laboratory of Chemical Engineering
Key Laboratory of Specially Functional Polymeric Materials and Related Technology (Ministry of Education)
Shanghai Key Laboratory of Multiphase Materials Chemical Engineering
East China University of Science and Technology
Shanghai 200237, P. R. China
E-mail: ylwang@ecust.edu.cn; zhanliang@ecust.edu.cn

Y. Zuo
Institute for New Energy Materials and Engineering/College of Materials Science and Engineering
Fuzhou University
Fuzhou 350108, P. R. China
E-mail: yinzezuo@fzu.edu.cn

X. Cheng, H. Lin, J. Wang
i-Lab & CAS Key Laboratory of Nanophotonic Materials and Device
Suzhou Institute of Nano-Tech and Nano-Bionics
Chinese Academy of Sciences
Suzhou 215123, P. R. China
E-mail: jian.wang@kit.edu

J. Zhang
School of Materials Science and Engineering
Xi'an University of Technology
Xi'an 710048, P. R. China

Y. Hu, J. Wang
Helmholtz Institute Ulm (HIU)
D89081 Ulm, Germany

Y. Hu, J. Wang
Karlsruhe Institute of Technology (KIT)
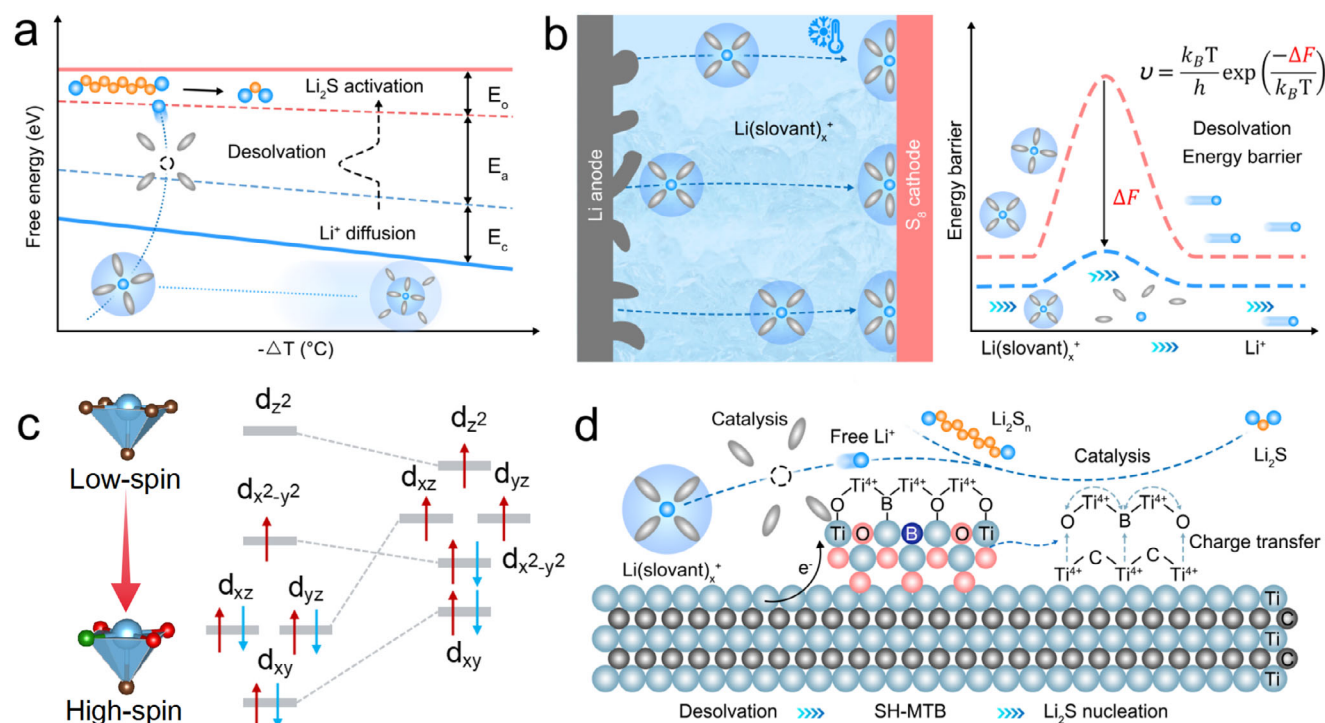D76021 Karlsruhe, Germany

Figure 1. a) Effect of operating temperature on energy barriers for Li ion transport in different processes; b) Illustration of batteries with three barriers of desolvation, diffusion and conversion, including the relationship between desolvation and operating temperature; c) Edge-delocalized electronic configurations of the 3d orbitals in catalysts for generating more active sites; d) Schematic diagram of cascade catalytic reaction on SH-MTB.

To deal with the above low-temperature issues, researchers always focus on the electrolyte engineering to extend the freezing point of designed electrolytes with diluted solvents.[13–15] Indeed, it works well without freezing but it tends to sacrifice the ion conductivity, which leads to the worse performance at higher rate.[16] Traditional electrolyte strategies often encounter challenges such as high cost, high viscosity, poor wettability, and electrolyte precipitation,[17–19] which further complicates the practical application of Li—S batteries. Alternatively, it is still necessary to extend the feasibility and possibility of commercial electrolyte down to low-temperature environment before freezing. As illustrated in Figure 1b, the carrier kinetics experience three steps from bulk electrolyte to interfacial desolvation and finally to electrode interior, exhibiting the tandem reactions and corresponding higher barriers. Decreasing the ion hopping energy (ΔF) is beneficial for promoting ion diffusion kinetics, and thus the electrocatalytic strategy might promote the dissociation of Li(solvents)$_x^+$ clusters and accelerate the diffusion kinetics of free Li ions, resulting in significant improvements of ion kinetics for faster reaction kinetics. However, nobody knows whether electrocatalysis works well in the tandem carrier kinetics at the sulfur/electrolyte side under low-temperature environment, which deserves to be comprehensively understood.

Recently, electron delocalization engineering has been proposed to redistribute the electronic density for generating more active sites.[20–23] Apart from the defect and atom catalysts, heterostructures composed of metal and semiconductors are also beneficial for electron redistribution and transfer, yielding maximum capability of catalysts at the interface.[24–27] However, the interface engineering effectively integrates multiphase via self-interaction.[28] Modulating the spin-state of electrons will indeed help to generate more active sites (Figure 1c). For example, MXene possesses high density at Fermi level, processing the exceptional electrical and mechanical properties.[29–31] Thus, the relationship between the edge-electron effect and desolvation/diffusion behaviors needs to be comprehensively understood.

Herein, the electron effect in the edge of catalysts is modulated and the corresponding strategy of self-transform Schottky heterojunction on MXene is proposed to achieve the edge delocalized electronic density. As a demo, the electron-delocalized MXene/TiO$_2$-based Schottky heterojunction with boron doping (SH-MTB) is designed and proposed as an electrochemical kinetic accelerator under low-temperature. Various characterizations of theoretical simulation, electrochemical evaluation as well as in situ sum frequency generation (SFG) have demonstrated that the cascade carrier kinetics are significantly increased by reducing the barriers of interfacial Li(solvents)$_x^+$ dissociation and further polysulfide conversions under low-temperature environment, offering high areal-capacity and fast charging/discharging capability at low-temperatures. Consequently, higher practical areal capacity (5.0 mAh cm^{-2}) and negligible self-discharge behaviors are achieved and the as-fabricated pouch cell with 200 mg$_s$ exhibits the areal capacity of 9.3 mAh cm^{-2} under a lean electrolyte amount (5 µL mg^{-1}), much better than state-of-art reports. Meanwhile, the electrochemical stability of Schottky heterostructure after cycling has been witnessed by electronic microscopies, spectroscopical measurement and X-ray tests, shedding light on
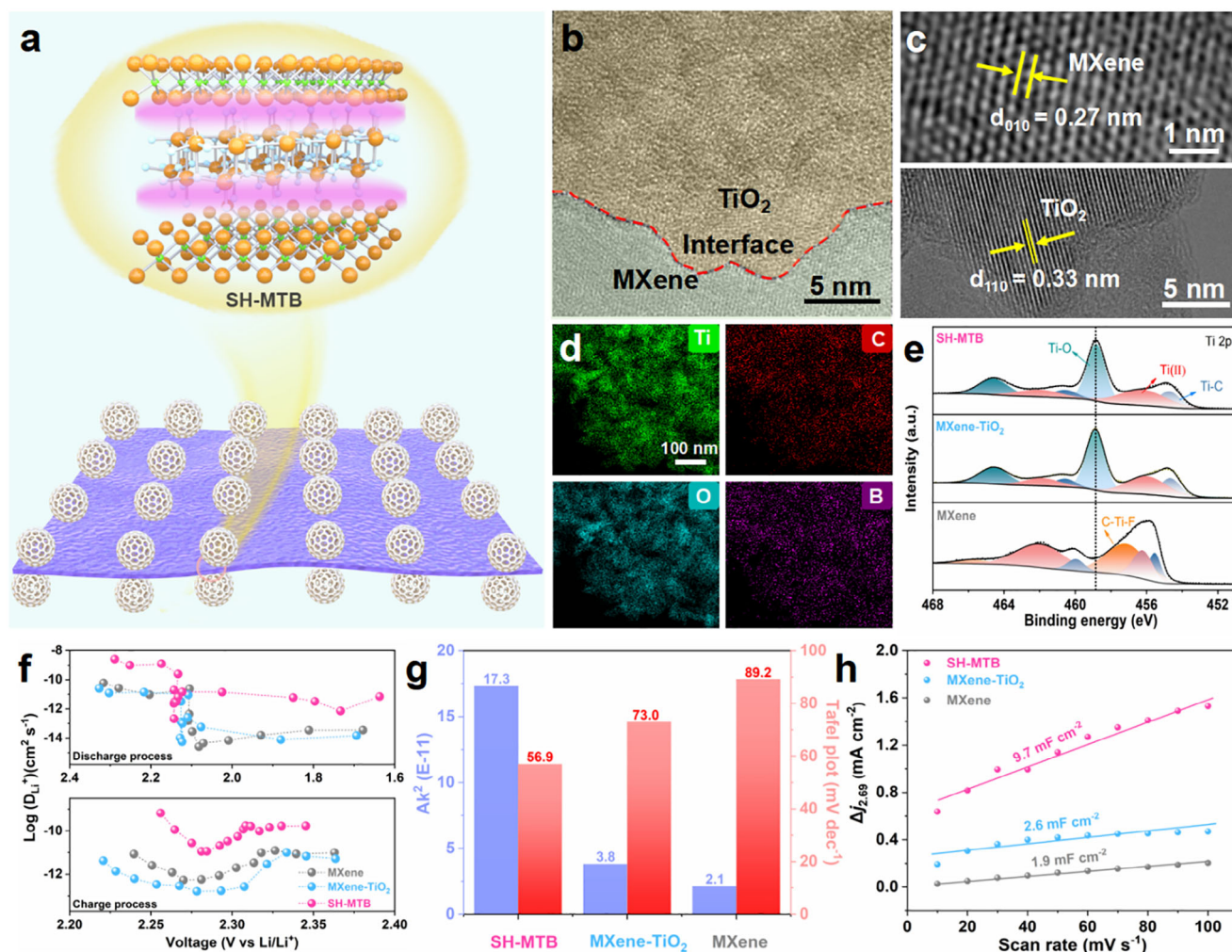
Figure 2. a) Schematic illustration of the delocalized electrons redistribution at the heterointerface of SH-MTB; b,c) High-resolution TEM images and d) elemental mapping results of SH-MTB; e) Ti 2p XPS of MXene, MXene-TiO$_2$ and SH-MTB; f) Li$^+$ diffusion coefficients calculated based on GITT curves; g) The Li$_2$S nucleation rates and Tafel slopes with different electrocatalysts; h) The relation of C$_{dl}$ currents to the scan rates at 2.69 V.

the practical application of Schottky heterostructure for accelerating the cascade carrier kinetics in Li metal battery under low-temperature.

2. Results and Discussion

As described in Figure 1c, the unique electron-donating or electron-withdrawing properties of Schottky environment elevate the overall 3d orbital energy level. Additionally, with the external boron doping, the occurrence of orbital spin splitting in SH-MTB drives electronic structure from a low-spin to a high-spin state, realizing edge-electron effect for generating more active sites at the interface. Figure 1d vividly illustrates the cascade catalytic processes propelled by the electron-delocalized catalysts. At the catalytic interface, the Li(solvents)$_x^+$ clusters experience rapid desolvation process to release free Li ion due to the fast charge transfer, while the released Li ion further participate in the sulfur conversion process to deposit abundant Li$_2$S at the neighboring Ti active

sites, improving the interconversion performance of Li—S batteries.

As a matter of concept, the self-transformed Schottky heterojunction was synthesized by self-templated method as exhibited in Figure S1 (Supporting Information), where it facilitated the delocalized electrons redistribution at the heterointerface (**Figure 2a**) for accelerating the cascade reactions of Li$^+$ desolvation, Li$^+$ diffusion and sulfur conversions. As shown in Figure S2 (Supporting Information), the SH-MTB heterostructure reveals a wrinkled morphology with uniformly distributed porous TiO$_2$ nanoparticles. The high-resolution transmission electron microscope (TEM) images (Figures 2b-c) depict the sharply defined heterointerfaces as indicated by red line, and the heterojunction of lattice stripe spacings of TiO$_2$ (110) with MXene (010) guarantees the rapid transfer of electrons/ions across the heterointerface. The uniformly porous structure is believed to enhance the dissociation capability toward Li(solvents)$_x^+$, offering significant advantages for further modulating the catalytic performance for sulfur evolution reactions.[32] Elemental mapping

2508225 (3 of 11)

ADVANCED
SCIENCE NEWS

www.advancedsciencenews.com

**ADVANCED
FUNCTIONAL
MATERIALS**

www.afm-journal.de

analysis of the SH-MTB composite convincingly showcases the uniform dispersion of Ti, C, O, and B elements (Figure 2d). The changes in energy bands are depicted in Figure S3 (Supporting Information). As the Fermi levels of the two components approach an equilibrium, electrons spontaneously move from conductive MXene to semiconductive TiO_2 once they intimately contact, generating the Schottky heterointerface. X-ray diffraction (XRD) patterns confirmed the crystal structure of SH-MTB heterostructure (Figure S4, Supporting Information), of which apparent (002) characteristic peak at 5.8° belongs to typical MXene. After self-transformation, new diffraction peaks appeared in the SH-MTB, assigned to TiO_2 (PDF No.84–1248) without any impurities. Besides, the Mott-Schottky plot (Figure S5, Supporting Information) also presents typical p–n heterostructure of the SH-MTB. The X-ray photoelectron spectroscopy (XPS) of Ti 2p spectra (Figure 2e) clearly exhibit obvious Ti─O and Ti─C bonds in the SH-MTB and MXene-TiO_2, indicating a C─Ti─O bridge is formed, which greatly affects the electronic structure. Importantly, compared to MXene, the Ti─C bond in SH-MTB exhibits a negative shift of ≈0.8 eV, confirming the electron transfer from MXene to B-doped TiO_2. In addition, strong intensity with g = 2.003 is observed at the electron paramagnetic resonance (EPR, Figure S6, Supporting Information) analysis of SH-MTB, which is attributed to the heterojunction with delocalized electrons by B-doping.

Then, the enhanced Li ion diffusion kinetics by different catalysts are further verified by galvanostatic intermittent titration technique (GITT) analysis, where the cell with SH-MTB presents the accelerated Li ion transport (Figure 2f) and the lowest polarization (190 vs 230 vs 200 mV, Figure S7, Supporting Information) during charge/discharge processes, agreeing well with the Li^+ diffusion coefficient in the full cell (Figure S8, Supporting Information). To evaluate carrier kinetics on polysulfide conversions, the UV–vis spectroscopy of Li_2S_6 solution after sufficient adsorption was performed and the intensity near 280 nm for SH-MTB experienced a more pronounced decline (Figure S9a, Supporting Information). As interpreted by XPS, the SH-MTB catalyst with Li_2S_6 adsorption (Figure S9b, Supporting Information) shows the peaks assigned to terminal sulfur (S_T^{-1}) and bridging sulfur (S_B^0) moving to higher binding energy. Furthermore, a distinct peak appeared at 455.6 eV can be attributed to Ti─S bonding, suggesting the existence of Lewis acid-base interaction between SH-MTB and Li_2S_6.[33] To witness the Li ion kinetics on liquid-solid conversion of LiPSs, cyclic voltammetry (CV) profiles of symmetric cells were explored (Figure S10, Supporting Information). The higher peak current and narrower voltage range demonstrate the fast conversion kinetics with the SH-MTB catalyst. Besides, the largest capacity of 311 mAh g^{-1} and the earliest peak at 1544 s of Li_2S precipitation accelerated by SH-MTB electrocatalyst were achieved with uniform and dense Li_2S precipitation morphology (Figures S11 and S12, Supporting Information), demonstrating the significantly enhanced Li_2S precipitation kinetics. Generally, the nucleation rate (A) and growth rate (k) of Li_2S are closely related to the corresponding response of Li_2S nucleation.[34] The value of Ak^2 experiences a significant enhancement by SH-MTB catalyst (Figure 2g), 8.4 and 4.6 times greater than others. The Tafel slopes associated with the conversions of S_8 to liquid Li_2S_x and subsequently to Li_2S were determined to be 54.7 and 56.9 mV dec^{-1} (Figure 2g; Figure S13,

Supporting Information), respectively, much lower than those with MXene (74.3 and 89.2 mV dec^{-1}) and MXene-TiO_2 (81.6 and 73.0 mV dec^{-1}), underscoring the enhanced catalytic capability of SH-MTB heterostructure. Additionally, the catalytic activity was further quantitatively assessed, where the SH-MTB gave rise to the largest C_{dl} value of 9.7 mF cm^{-2} (Figure 2h; Figure S14, Supporting Information), almost four times higher than others, indicating the largest electrochemical active surface area provided by electron-delocalization of SH-MTB.

Given that the desolvation process takes place at the electrode/electrolyte interface, efficiently promoting the dissociation of $Li(solvents)_x^+$ clusters to give off free Li ions is pivotal in enhancing and uniformizing the Li^+ mobility. To disclose the $Li(solvents)_x^+$ desolvation process, in situ interface-selective sum frequency generation (SFG) spectroscopy based on an asymmetrical interface was carried out to dynamically track the interface evolutions, as illustrated in Figure S15 (Supporting Information). **Figure 3a** schematically displays the state changes of $Li(solvents)_x^+$ species at the electrode/electrolyte interface with/without external electrical field. Typically, the interfacial behaviors are intimately related to the electrode surface status and distinct C─H bond vibrations are observed in the region of 2750–3050 cm^{-1}, suggesting the existence of solvated solvent molecules at the interface (Figure 3b,c; Figure S16, Supporting Information).[35–37] In comparison to the adsorption state of solvent at open-circuit potential (OCP) status, different adsorption behaviors of $Li(solvents)_x^+$ are shown on the surface of SH-MTB, indicating the different inner Helmholtz plane layer near the electrode. Along with the strength of external electrical field, the solvent signals on the surfaces of MXene-TiO_2 and MXene systems increase significantly, suggesting more $Li(solvents)_x^+$ clusters aggregate at the interface driven by electrical field. In sharp contrast, adsorption states behave conversely when the bias voltage was increased to 50 mV at the SH-MTB//electrolyte interface, indicating the presence of inner built-in electrical field (BIEF) of SH-MTB. Meanwhile, the peak intensities of C─H vibrations decrease along with the enhancement of electrical field, which is undoubtedly attributed to the rapid dissociation of the Li^+-solvent complex catalyzed by SH-MTB. As depicted in Figure S17 (Supporting Information), the $Li(solvents)_x^+$ adsorption behavior is subjected to the combined effect of internal and external electric fields, and the characteristic peaks of the solvent molecules experience an obvious inversion, demonstrating the initial stage of dynamic dissociation toward Li^+-solvents.

Meanwhile, the Raman spectroscopy also investigates the bulk solvation structure of Li ions (Figure 3d; Figure S18, Supporting Information). Generally, three types of solvent-separated ion pairs (SSIPs), contact ion pairs (CIP), and aggregates (AGGs) are presented. Specifically, the total ratio of "AGG + CIP" increases from 58% in MXene to 91% in SH-MTB, robustly suggesting the superior desolvation capability of SH-MTB electrocatalyst.[38] The aforementioned spectroscopic findings clearly demonstrate that the catalytic strategy efficiently facilitates the breakdown of the $Li(solvents)_x^+$ cluster to liberate a substantial quantity of free Li ions at the interface. Consequently, this accelerated desolvation allows an improvement of the Li^+ transference number, rising from 0.33 for MXene to 0.58 for SH-MTB (Figure 3e; Figure S19, Supporting Information), nearly two times higher than that on pristine MXene. In short, Figure 3f depicts interfacial evolution
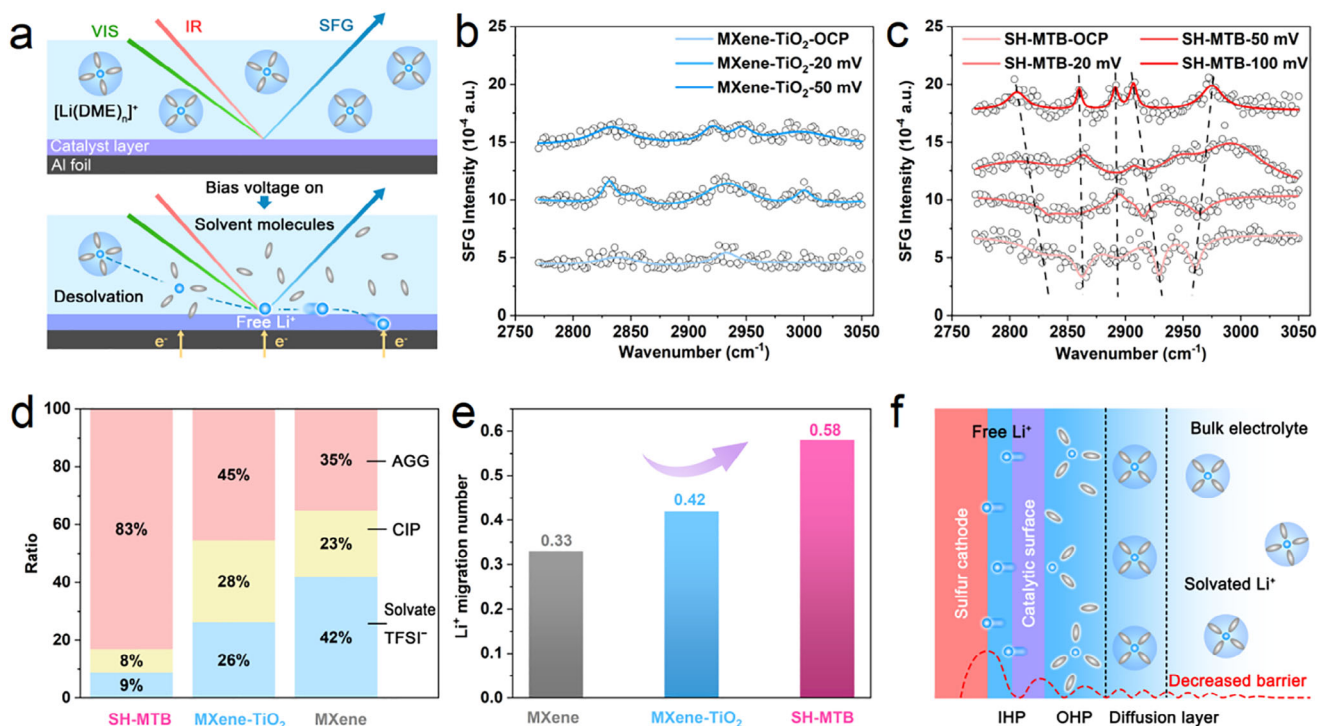
ADVANCED
SCIENCE NEWS

www.advancedsciencenews.com

ADVANCED
FUNCTIONAL
MATERIALS

www.afm-journal.de

Figure 3. a) The molecular states of Li$^+$ solvation structure at the SH-MTB electrode/electrolyte interface before and after bias voltage; The SFG spectra of different adsorption states of the Li$^+$ solvation structure in electrolyte with b) MXene-TiO$_2$ and c) SH-MTB catalysts; d) The ratio summary of SSIP, CIP, and AGG in different systems; e) Li ion transference number in different systems; f) Interfacial evolution of the double electric layer near the sulfur cathode induced by SH-MTB catalyst, changing the inner Helmholtz plane.

at the sulfur cathode/electrolyte interface with/without catalysts. In the bulk electrolyte, Li ions in the solvated structure fill the outer Helmholtz plane (OHP) layer and dissociate upon entering the inner Helmholtz plane (IHP) layer. While, it behaves differently when introducing catalyst at the interface. The partial or completed dissociated Li(solvents)$_x^+$ species dominates in the IHP layer, as comprehensively understood by above spectroscopical analysis. Consequently, the desolvation energy barrier and the trans-interfacial transport energy barrier of Li ions are greatly reduced to benefit more dissociative Li$^+$, which accelerates the conversion reaction between Li ions and polysulfides, thus suppressing the shuttle effect.

To gain the deeper insights of cascade carrier kinetics propelled by Schottky heterostructure, the density functional theory (DFT) was further intimated. As shown in **Figure 4**a, the charge density difference reveals a significant charge redistribution occuring at the interface of SH-MTB, where the electrons (0.87 e$^-$) transfer from Ti atoms on MXene to neighboring O atoms on TiO$_2$, establishing a BIEF to modulate the electronic density of polysulfide with moderate adsorption energy for redox reaction (Figure 4b,c; Figures S20–S23, Supporting Information). The accelerated electron movement to the surface of SH-MTB catalyst enhances the carrier transport. Specifically, the electron localization function (ELF) in Figure 4d and charge density difference (Figure S24, Supporting Information) further demonstrate the heteroatom of B in SH-MTB is more favorable for generating electron delocalization at the heterointerface, suggesting d-orbital electron redistributions. Moreover, the density of state

(DOS) in Figure 4e and Figure S25 (Supporting Information) provides that the Schottky heterojunction has the decreased d-orbital electrons of Ti on MXene while the d-orbital electrons of Ti on TiO$_2$ is increased in comparison to other substances, indicating the electron migration in the metal-semiconductor interface and endowing the SH-MTB with better electronic conductivity than individual MXene and TiO$_2$.

As mentioned before, the sulfur redox conversions contain three steps: 1) Li(solvents)$_x^+$ dissociation; 2) Free Li ion transport across the electrolyte/sulfur cathode interface; 3) Li ion entering reactions in the sulfur interior. For simplification, the Li(DME)$_4^+$ cluster was selected as the outer solvation shell owing to the stronger interaction between 1,2-dimethoxyethane (DME) and Li$^+$, as compared to solvent molecules such as 1,3-dioxolane (DOL).[39–41] To elucidate catalytic function of the SH-MTB, the energy barrier toward dissociation evolutions of Li(DME)$_4^+$ were imitated and calculated. As exhibited in Figure 4f, the desolvation barriers increase along with more solvent coordination around Li$^+$ in the both systems. For example, dissociating Li(DME)$_3^+$ into Li(DME)$_2^+$ and Li$^+$ will cost the energy of 0.83 eV, while only 0.63 eV is needed on the surface of SH-MTB, clearly demonstrating the superior electrocatalytic ability for reaching more Li ions. To comprehensively understand the desolvation process in pristine electrolyte or SH-MTB surface, the molecular dynamics (MD) simulation was employed to evaluate the coordination surroundings, as exhibited in Figure 4g and Figure S26 (Supporting Information). The radial distribution functions (RDF) were used to demonstrate the average local solvent-solute interaction state
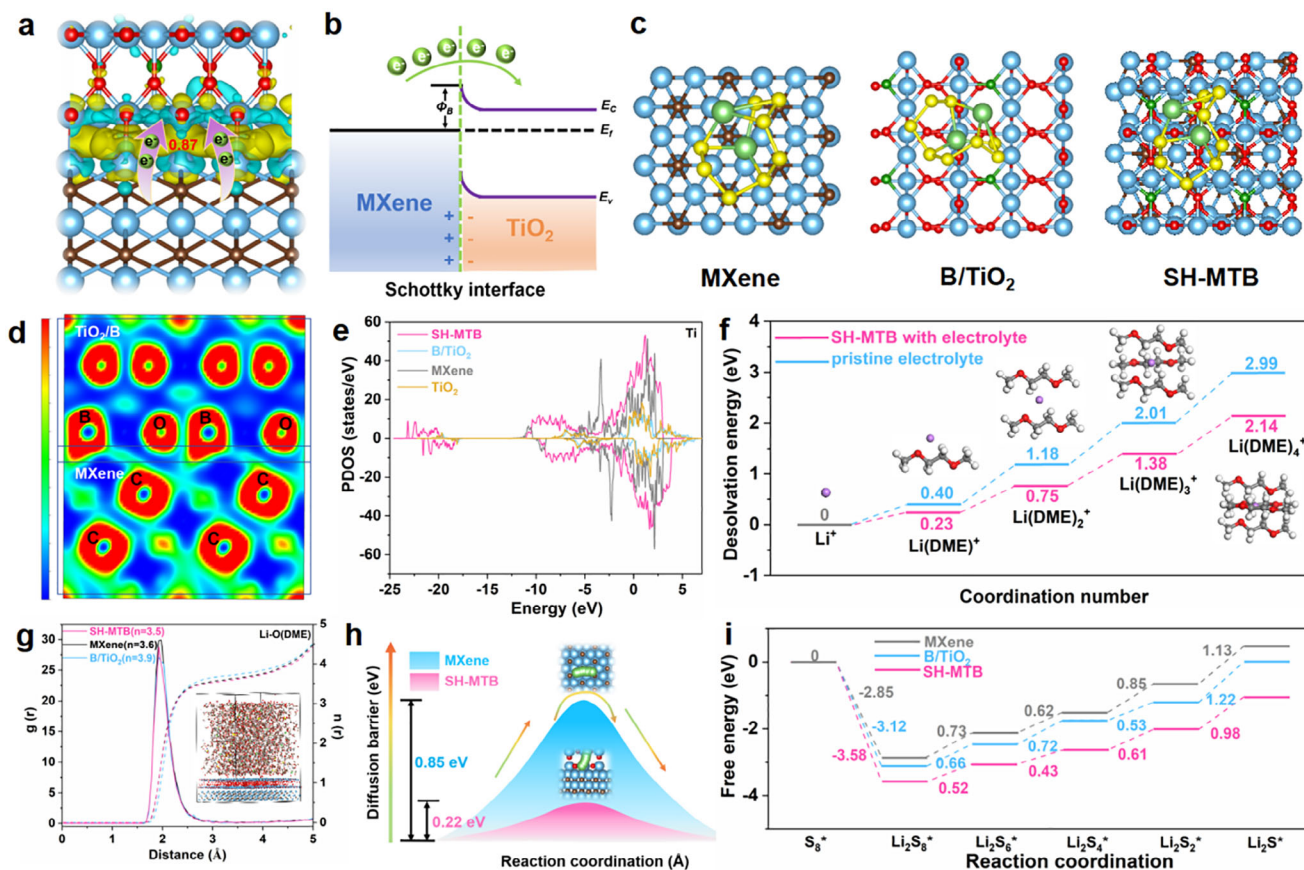
Figure 4. a) The charge density difference of SH-MTB; b) Schematic illustration of SH-MTB with electron delocalization; c) The geometry optimized structures of Li_2S_8 adsorbed on different catalysts; d) 2D electronic local function of SH-MTB. e) The DOS of MXene, TiO_2, B/TiO_2 and SH-MTB; f) The desolvation energy of $Li(DME)_x^+$ in different systems; g) Radial distribution functions of O (DME) with respect to Li^+ in different systems; h) Li^+ migration pathways and migration energy barriers in SH-MTB or MXene. i) The Gibbs free energy changes of the conversions of sulfur species on TiO_2, B/TiO_2 and SH-MTB.

in different electrolyte systems. In comparison to the coordination number of ≈4 in the bulk pristine electrolyte, the solvent-solute interaction weakens and the coordination number of Li^+-DME exhibits a significant decrease to 3.5 by the catalysis of SH-MTB. Meanwhile, the encouraging desolvation process also brings about favorable Li^+ migration kinetics (Figure 4h), due to obviously decreased diffusion barrier accounting for one forth on that of MXene (0.22 vs 0.85 eV), significantly evidencing the SH-MTB to promote ion diffusion across the interface. To further explore the sulfur conversion kinetics on SH-MTB catalyst, the Gibbs free energy differences related to various sulfur conversions were calculated and compared. The results in Figure 4i reveal the lowest Gibbs free energy changes in rate-determining steps by SH-MTB, suggesting a superb electrocatalytic effect for polysulfide conversions in inhibiting shuttling.[42]

The excellent carrier kinetics accelerated by SH-MTB were also investigated in the Li—S full cells. Cycled at 0.2 C (**Figure 5a**; Figure S27, Supporting Information), the cell assembled with SH-MTB exhibits an initial capacity of 1355 mAh g^{-1} and then stabilizes at 945 mAh g^{-1} after 200 cycles. In comparison, the cells with MXene and MXene-TiO$_2$ both undergo rapid capacity declines. Further increasing the current rate to 4 C, the capac-

ities decrease gradually and the cell with SH-MTB stabilized at 961, 858, and 743 mAh g^{-1} at 1, 3 and 4 C, respectively, surpassing those cells with MXene and MXene-TiO$_2$ at the same rate (Figure 5b; Figure S28, Supporting Information). The smallest charge transfer resistance for SH-MTB well explain the superior rate performance (Figure S29, Supporting Information). Moreover, the long-term cycling stability with SH-MTB reveals an attenuation rate of 0.041% per cycle over 1000 cycles at 1 C, much better than previous reported works (Figures 5c; Figure S30, Supporting Information).[43–55]

For the practical application requirement, the high sulfur-loading cathode or low-temperature surrounding are the major obstacles of Li—S batteries. Impressively, the cell with SH-MTB demonstrates an initial areal capacity of 7.8 mAh cm^{-2} at 0.1 C and keeps a substantial areal capacity of 4.8 mAh cm^{-2} after 100 cycles (Figure S31, Supporting Information), far exceeding the requirements of commercial Li ion batteries. When the temperature shifts down to 0 °C, the majority of Li batteries always exhibit impaired capabilities owing to the severe solvation shell and sluggish diffusion. To confirm the robust carrier kinetics of SH-MTB electrocatalyst toward temperature, the adaptability of the cell under low-temperatures was evaluated. Notably, a remarkable
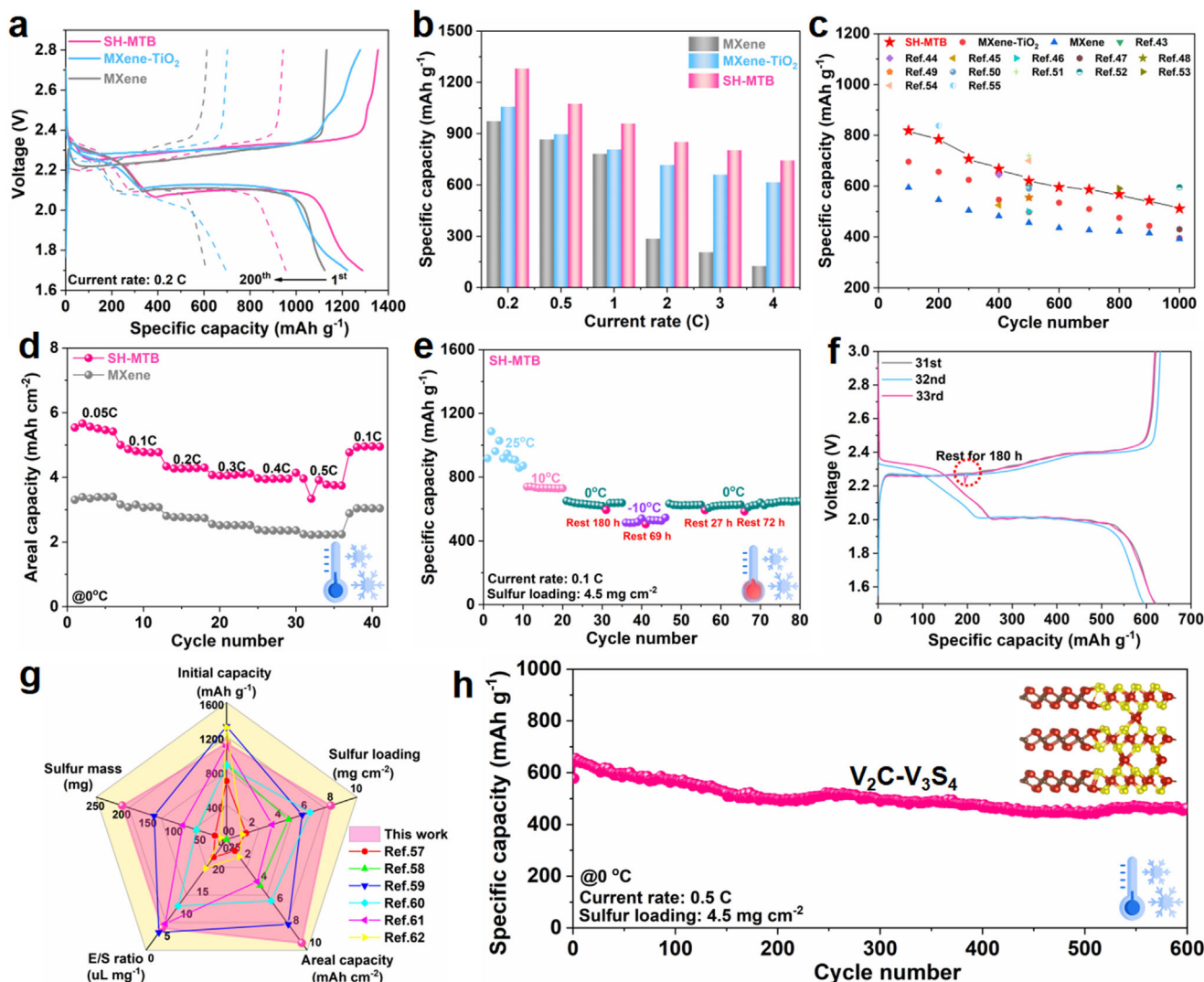
Figure 5. a) Voltage profiles at 0.2 C and b) rate performance of the cells with MXene, MXene-TiO_2 and SH-MTB; c) Comparison of long-term cycling stability at 1 C between SH-MTB and ever reported Li—S batteries; d) Rate performance of high-loading sulfur cathode operated at 0 °C with SH-MTB and MXene; e) Cycling stability at 0.1 C with varying operation temperatures and f) the voltage profiles before and after 180 h resting at 0 °C; g) Comparison of the pouch cell results with state-of-art reports; h) Cycling performance with extended V_2C-V_3S_4 Schottky heterostructure under low-temperature environment.

capacity of 668 mAh g^{-1} was achieved at 2 C (Figure S32, Supporting Information). Even reduced to −10 °C, the cell with SH-MTB kept 740 mAh g^{-1} after 200 cycles (Figure S33, Supporting Information) and a high capacity of 628 mAh g^{-1} was still achieved when switching to 0.2 C, confirming favorable desolvation and diffusion at low-temperature.

Unfortunately, high-loading performance of Li—S batteries at low-temperatures has rarely been studied due to their intricate desolvation and sluggish redox reactions.[56] Excitingly, the SH-MTB offers the high-loading sulfur cathode with a high areal capacity of 5.0 mAh cm^{-2} at 0 °C (Figure S34, Supporting Information) and stabilizes for more than 60 cycles. Meanwhile, the high-loading sulfur cathode (≈5 mg cm^{-2}) with SH-MTB also displays impressive rate performance under low-temperature (Figure 5d). Even at 0.5 C, a high reversible areal capacity of ≈3.8 mAh cm^{-2} and well-preserved charge/discharge platforms were obtained (Figure S35, Supporting Information). Switching current rate back to 0.1 C, the capacity recovered to original capacity value, highlighting the exceptional reaction kinetics of the SH-MTB electrocatalyst under lower temperatures and high mass loadings. Further, the behaviors of high-loading sulfur cathode with SH-MTB under wide temperature from room temperature of 25 to −10 °C were investigated (Figure 5e; Figure S36, Supporting Information). Even reduced to −10 °C, the high-loading sulfur cathode can still maintain the capacity of 2.4 mAh cm^{-2}. Notably, the self-discharge investigation by resting for 180 h remains the same capacity with little change in the voltage profiles (Figures 5f), indicating the fast carrier kinetics toward polysulfides shuttling. Li—S pouch cell was also assembled with SH-MTB catalyst to pursue promising potential. It delivers a high initial areal capacity of 9.36 mAh cm^{-2} even under high areal sulfur loading of 8.0 mg cm^{-2} (total mass: ≈200 mg) and a low E/S

**ADVANCED
SCIENCE NEWS**

www.advancedsciencenews.com

**ADVANCED
FUNCTIONAL
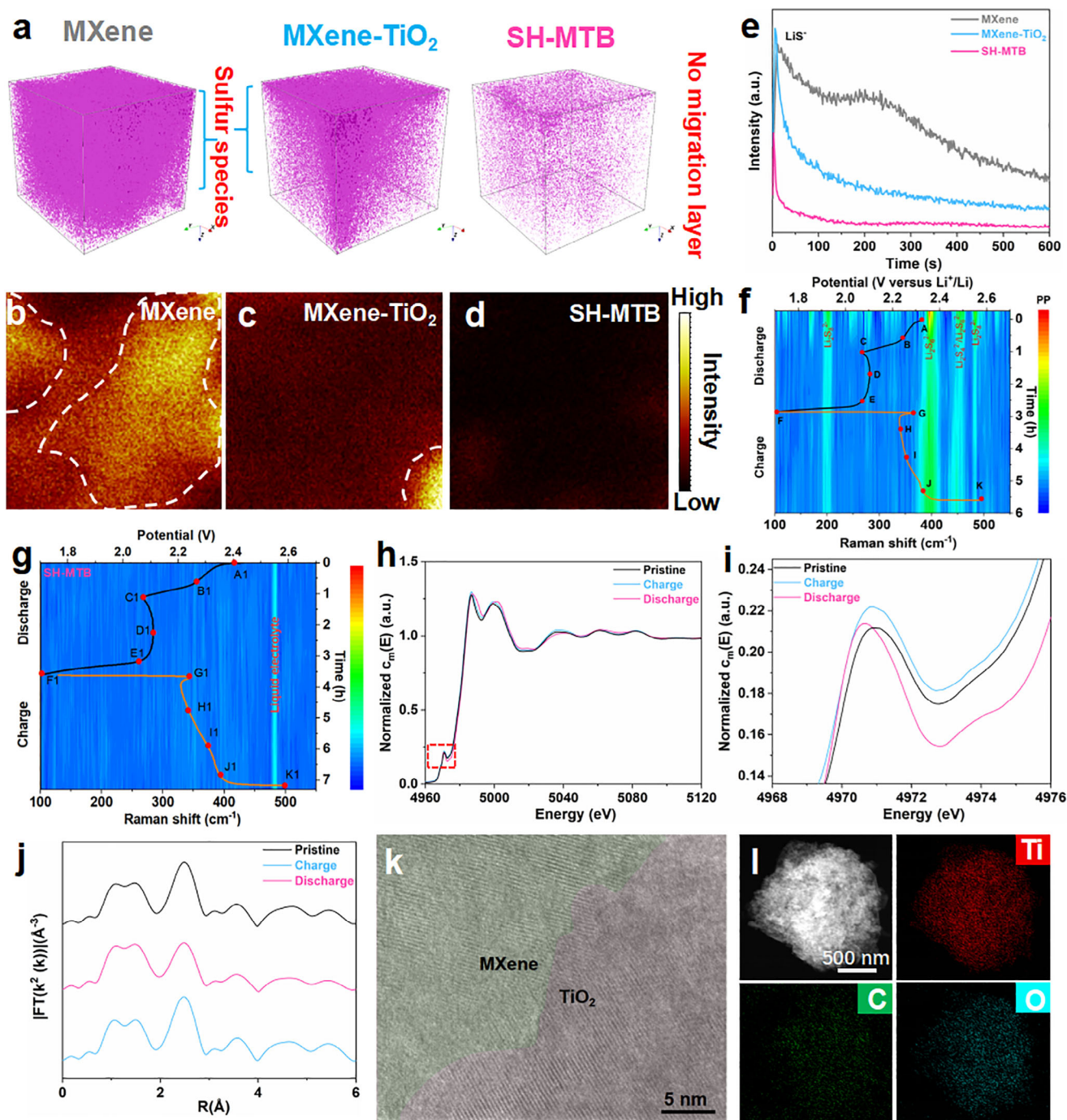MATERIALS**

www.afm-journal.de

Figure 6. a) 3D rendering reconstruction and b–d) 2D secondary-ions distribution images of S species in cycled separator with different catalysts, and corresponding e) LiS⁻ depth profiles; In situ time-resolved Raman image of the cell with f) PP and g) SH-MTB modified separator; h) Ex-situ XANES spectra and i) corresponding localized enlargement; j) Fourier transformed curves of the Ti K-edge EXAFS spectra of SH-MTB catalyst in different states; k) High-resolution TEM image and l) corresponding mapping results of the cycled SH-MTB.

ratio of 5.0 µL mg⁻¹ (Figure S37, Supporting Information). The electrochemical Li–S pouch cell in this work demonstrated an exceptionally superior level compared to recently-reported works (Figure 5g; Table S1, Supporting Information).[57–62] After cycling for more than 50 cycles, an impressive areal capacity of ≈5 mAh cm⁻² with obvious discharge/charge plateau is also maintained

(Figure S38, Supporting Information), showing highly accelerated desolvation and redox kinetics in practical pouch cell applications. In addition, this Schottky heterostructure can be further extended to other MXene-based heterojunction such as V_2C-V_3S_4 (Figure S39, Supporting Information), and the high desolvation degree of electrolyte with the help of V_2C-V_3S_4 is obtained,

**ADVANCED
SCIENCE NEWS**

www.advancedsciencenews.com

**ADVANCED
FUNCTIONAL
MATERIALS**

www.afm-journal.de

suggesting the exceptional catalytic desolation performance. Consequently, the high mass loading sulfur cathode with V_2C-V_3S_4 keeps capacities of 4.8 and 3.3 mAh cm^{-2} after 100 cycles at 0.1 C under both ambient (25 °C) and low-temperatures (0 °C) (Figure S40, Supporting Information). Even at 0.5 C, the high-loading sulfur cathode stabilizes for over 600 cycles under 0 °C (Figure 5h), further manifesting the effective catalytic capability for desolation and conversions by the electron delocalization even under low-temperature surrounding.

To elucidate the stability and underlying mechanisms of SH-MTB electrocatalyst, the time-of-flight secondary ion mass spectrometry (TOF-SIMS) and in situ Raman were employed. **Figure 6**a-d provide 2D and 3D signals of sulfur-related species in the cycled separators. As shown in the 3D rendering reconstruction images, the S signal gradually weakens as the depth increases for the cycled SH-MTB@PP, agreeing well with the LiS$^-$ depth profiles in Figure 6e, while the S signal for the cycled MXene@PP and MXene-TiO$_2$@PP exhibits high concentration. Besides, in the 2D secondary-ions distribution images, the cycled SH-MTB@PP exhibits the less amount of Li$_2$S, implying the migration of sulfur species is well inhibited by the SH-MTB owing to its superior Li$^+$ desolation and completed sulfur redox conversions.[63] In situ Raman spectroscopy was also utilized to inspect the inhibition of shuttling effect by SH-MTB. In comparison with the pristine system where obvious peaks at 398, 450, 200 and 450 cm^{-1} are detected attributed to long-chain S$_6^{2-}$ and the short-chain S$_4^{2-}$ (Figure 6f; Figure S41a, Supporting Information),[64] the Raman signal of LiPSs becomes nearly undetectable (Figure 6g; Figure S41b, Supporting Information) in the charge and discharge processes for the SH-MTB system, further demonstrating the diffusion of LiPSs is efficiently blocked and the sulfur species are promptly converted on the cathode side, agreeing well with the denser and smoother morphology of cycled Li anode (Figure S42, Supporting Information).[65–67]

Afterward, the electrochemical stability of cycled SH-MTB electrocatalyst was further inspected by X-ray measurements and electronic microscopies. To confirm the chemical surroundings of the cycled SH-MTB, the Ti K-edge X-ray absorption fine structure (XAFS) spectra are performed on catalyst in different electrochemical states. As displayed in Figure 6h-i, the Ti K-edge X-ray absorption near-edge structure (XANES) spectra of SH-MTB reveals slight change happens on the SH-MTB catalyst, indicating the surrounding vibration of chemical environment between SH-MTB and Li$_2$S. Recovering to charging state, the little change in valence and coordination structures of SH-MTB disappears (Figure 6j), which is consistent with the pristine states, further validating the structural stability of SH-MTB during cycling. Moreover, the SH-MTB still preserves pristine morphology after repeated charge-discharge processes, the heterogeneous interface of SH-MTB is retained (Figure 6k) with the corresponding energy dispersive spectroscopy (EDS) mapping results of homogenous distributions of each element (Figure 6l), implying the stability and robustness of the SH-MTB electrocatalyst.

3. Conclusion

In summary, to achieve fast Li$^+$ desolation to promote rapid sulfur conversion kinetics, the edge-delocalized electron effect of catalysts is initially proposed and the self-transformed fabrication method with adjustable electronic density is designed. Combined various characterizations of theoretical simulation, electrochemical evaluation as well as in situ sum frequency generation (SFG), the SH-MTB demonstrates that the cascade carrier kinetics are significantly increased by reducing the interfacial Li(solvents)$_x^+$ dissociation for further polysulfide redox conversions, acquiring high kinetics at low-temperatures. Consequently, the high-loading sulfur cathode with SH-MTB exhibited a high areal capacity of 5.0 mAh cm^{-2}, an outstanding rate capability (3.8 mAh cm^{-2} at 0.5 C) under various low-temperature environments, exhibiting the robust electrochemical stability of the SH-MTB catalyst as indicated by X-ray measurements and electronic microscopies. Impressively, a punch cell with 8 mg cm^{-2} (total mass 200 mg) stabilizes for more than 50 cycles and maintains the areal capacity of 4.9 mAh cm^{-2} under lean electrolyte condition, much better than most reports. Our work showcases the practical application for modulating the edge electrons of catalyst for achieving robust low-temperature batteries.

Conflict of Interest

The authors declare no conflict of interest.

Data Availability Statement

The data that support the findings of this study are available from the corresponding author upon reasonable request.

[1] J. Xu, H. Zhang, F. Yu, Y. Cao, M. Liao, X. Dong, Y. Wang, *Angew. Chem., Int. Ed.* **2022**, *61*, 202211933.

[2] L. Zeng, J. Zhu, P. K. Chu, L. Huang, J. Wang, G. Zhou, X. F. Yu, *Adv. Mater.* **2022**, *34*, 2204636.

[3] X. Zuo, L. Wang, M. Zhen, T. You, D. Liu, Y. Zhang, *Angew. Chem., Int. Ed.* **2024**, *63*, 202408026.

[4] J. Gu, Y. Zhang, Y. Shi, Y. Jin, H. Chen, X. Sun, Y. Wang, L. Zhan, Z. Du, S. Yang, M. Li, *ACS Nano* **2024**, *18*, 25966.

[5] Y. Zhao, C. Geng, L. Wang, Y. Cao, H. Yang, L. Peng, X. Jiang, Y. Guo, X. Ye, W. Lv, Q.-H. Yang, *Natl. Sci. Rev.* **2024**, *11*, nwae190.

[6] W. Lim, S. Kim, C. Jo, J. Lee, *Angew. Chem., Int. Ed.* **2019**, *58*, 18746.

[7] P. Wang, B. Xi, S. Xiong, *Acc. Chem. Res.* **2024**, *57*, 2093.

[8] J. Wang, L. Li, H. Hu, H. Hu, Q. Guan, M. Huang, L. Jia, H. Adenusi, K. V. Tian, J. Zhang, S. Passerini, H. Lin, *ACS Nano* **2022**, *16*, 17729.

[9] M. Du, P. Geng, C. Pei, X. Jiang, Y. Shan, W. Hu, L. Ni, H. Pang, *Angew. Chem., Int. Ed.* **2022**, *61*, 202209350.

[10] L. P. Hou, Z. Li, N. Yao, C. X. Bi, B. Q. Li, X. Chen, X. Q. Zhang, Q. Zhang, *Adv. Mater.* **2022**, *34*, 2205284.

[11] S. C. Kim, X. Gao, S.-L. Liao, H. Su, Y. Chen, W. Zhang, L. C. Greenburg, J.-A. Pan, X. Zheng, Y. Ye, M. S. Kim, P. Sayavong, A. Brest, J. Qin, Z. Bao, Y. Cui, *Nat. Commun.* **2024**, *15*, 1268.

[12] J. Wang, J. Zhang, S. Duan, L. Jia, Q. Xiao, H. Liu, H. Hu, S. Cheng, Z. Zhang, L. Li, W. Duan, Y. Zhang, H. Lin, *Nano Lett.* **2022**, *22*, 8008.

[13] H. Ji, Z. Wang, Y. Sun, Y. Zhou, S. Li, J. Zhou, T. Qian, C. Yan, *Adv. Mater.* **2023**, *35*, 2208590.

[14] P. Xiao, X. Yun, Y. Chen, X. Guo, P. Gao, G. Zhou, C. Zheng, *Chem. Soc. Rev.* **2023**, *52*, 5255.

[15] Z. Jiang, Z. Zeng, W. Hu, Z. Han, S. Cheng, J. Xie, *Energy Storage Mater.* **2021**, *36*, 333.

[16] X. Song, X. Liang, H. Kim, Y.-K. Sun, *ACS Energy Lett.* **2024**, *9*, 5576.

[17] L. Wang, Y. Ye, N. Chen, Y. Huang, L. Li, F. Wu, R. Chen, *Adv. Funct. Mater.* **2018**, *28*, 1800919.

[18] Y. Liu, Y. Elias, J. Meng, D. Aurbach, R. Zou, D. Xia, Q. Pang, *Joule* **2021**, *5*, 2323.

[19] S. Yuan, T. Kong, Y. Zhang, P. Dong, Y. Zhang, X. Dong, Y. Wang, Y. Xia, *Angew. Chem., Int. Ed.* **2021**, *60*, 25624.

[20] P. Chen, T. Wang, D. He, T. Shi, M. Chen, K. Fang, H. Lin, J. Wang, C. Wang, H. Pang, *Angew. Chem., Int. Ed.* **2023**, *62*, 202311693.

[21] Z. Zhao, Y. Pan, S. Yi, Z. Su, H. Chen, Y. Huang, B. Niu, D. Long, Y. Zhang, *Adv. Mater.* **2024**, *36*, 2310052.

[22] K. Li, T. Li, Z. Wang, K. Shi, Y. Sun, J. Li, J. Ren, A. Lu, X. Li, Q. Liu, *Adv. Funct. Mater.* **2024**, *34*, 2410517.

[23] Y. Jiang, Y.-P. Deng, R. Liang, N. Chen, G. King, A. Yu, Z. Chen, *J. Am. Chem. Soc.* **2022**, *144*, 4783.

[24] T. Wang, J. He, Z. Zhu, X. B. Cheng, J. Zhu, B. Lu, Y. Wu, *Adv. Mater.* **2023**, *35*, 2303520.

[25] Y. Li, T. Li, Y. Deng, W. Tang, H. Wu, M. Feng, P. Yan, R. Liu, *Small* **2024**, *20*, 2401921.

[26] Y. Deng, W. Tang, Y. Zhu, J. Ma, M. Zhou, Y. Shi, P. Yan, R. Liu, *Small Methods* **2023**, *7*, 2300186.

[27] Y. Deng, J. Yang, Z. Qiu, W. Tang, Y. Li, Q. Wang, R. Liu, *Small* **2024**, *8*, 2301316.

[28] Y. Guo, Q. Niu, F. Pei, Q. Wang, Y. Zhang, L. Du, Y. Zhang, Y. Zhang, Y. Zhang, L. Fan, Q. Zhang, L. Yuan, Y. Huang, *Energy Environ. Sci.* **2024**, *17*, 1330.

[29] L. Chen, Y. Sun, X. Wei, L. Song, G. Tao, X. Cao, D. Wang, G. Zhou, Y. Song, *Adv. Mater.* **2023**, *35*, 2300771.

[30] Y. Shi, Z. Du, S. Yang, *Adv. Funct. Mater.* **2024**, *34*, 2404653.

[31] C. Tsounis, P. Kumar, H. Masood, R. Kulkarni, G. Gautam, C. Müller, R. Amal, D. Kuznetsov, *Angew. Chem., Int. Ed.* **2023**, *62*, 202210828.

[32] X. Zhang, X. Li, Y. Zhang, X. Li, Q. Guan, J. Wang, Z. Zhuang, Q. Zhuang, X. Cheng, H. Liu, J. Zhang, C. Shen, H. Lin, Y. Wang, L. Zhan, L. Ling, *Adv. Funct. Mater.* **2023**, *33*, 2302624.

[33] V. P. Nguyen, J. S. Park, H. C. Shim, J. M. Yuk, J. H. Kim, D. Kim, S. M. Lee, *Adv. Funct. Mater.* **2023**, *33*, 2303503.

[34] X. Li, Y. Zuo, Y. Zhang, J. Wang, Y. Wang, H. Yu, L. Zhan, L. Ling, Z. Du, S. Yang, *Adv. Energy Mater.* **2024**, *14*, 2303389.

[35] Q. Guan, J. Wang, Q. Zhuang, J. Zhang, L. Li, L. Jia, Y. Zhang, H. Hu, H. Hu, S. Cheng, H. Zhang, H. Li, M. Liu, S. Wang, H. Lin, *Energy Environ. Sci.* **2024**, *17*, 3765.

[36] J. Wang, J. Zhang, J. Wu, M. Huang, L. Jia, L. Li, Y. Zhang, H. Hu, F. Liu, Q. Guan, M. Liu, H. Adenusi, H. Lin, S. Passerini, *Adv. Mater.* **2023**, *35*, 2302828.

[37] J. Wang, H. Liu, J. Zhang, Q. Xiao, C. Wang, Y. Zhang, M. Liu, Q. Kang, L. Jia, D. Wang, Q. Li, W. Duan, H. Adenusi, S. Passerini, Y. Zhang, H. Lin, *Energy Storage Mater.* **2024**, *67*, 103289.

[38] L. Li, H. Tu, J. Wang, M. Wang, W. Li, X. Li, F. Ye, Q. Guan, F. Zhu, Y. Zhang, Y. Hu, C. Yan, H. Lin, M. Liu, *Adv. Funct. Mater.* **2023**, *33*, 2212499.

[39] X. Miao, C. Song, W. Hu, Y. Ren, Y. Shen, C. Nan, *Adv. Mater.* **2024**, *36*, 2401473.

[40] J. Wu, Z. Gao, Y. Tian, Y. Zhao, Y. Lin, K. Wang, H. Guo, Y. Pan, X. Wang, F. Kang, N. Tavajohi, X. Fan, B. Li, *Adv. Mater.* **2023**, *35*, 2303347.

[41] R. Cao, J. Chen, K. S. Han, W. Xu, D. Mei, P. Bhattacharya, M. H. Engelhard, K. T. Mueller, J. Liu, J. G. Zhang, *Adv. Funct. Mater.* **2016**, *26*, 3059.

[42] D. R. Deng, H. J. Xiong, Y. L. Luo, K. M. Yu, J. C. Weng, G. F. Li, J. Lei, Y. Li, M. S. Zheng, Q. H. Wu, *Adv. Mater.* **2024**, *36*, 2406135.

[43] D. Lu, X. Wang, Y. Hu, L. Yue, Z. Shao, W. Zhou, L. Chen, W. Wang, Y. Li, *Adv. Funct. Mater.* **2023**, *33*, 2212689.

[44] Y. Li, Y. Deng, J. L. Yang, W. Tang, B. Ge, R. Liu, *Adv. Funct. Mater.* **2023**, *33*, 2302267.

[45] D. Zhang, T. Duan, Y. Luo, S. Liu, W. Zhang, Y. He, K. Zhu, L. Huang, Y. Yang, R. Yu, X. Yang, H. Shu, Y. Pei, X. Wang, M. Chen, *Adv. Funct. Mater.* **2023**, *33*, 2306578.

[46] W. Xia, Y. Chen, M. Han, X. Wu, H. Yang, K. Fu, M. Chen, X. Wang, H. Shu, *Adv. Funct. Mater.* **2024**, *34*, 2400262.

[47] C. Zhao, Y. Huang, B. Jiang, Z. Chen, X. Yu, X. Sun, H. Zhou, Y. Zhang, N. Zhang, *Adv. Energy Mater.* **2024**, *14*, 2302586.

[48] Y. Kong, L. Wang, M. Mamoor, B. Wang, G. Qu, Z. Jing, Y. Pang, F. Wang, X. Yang, D. Wang, L. Xu, *Adv. Mater.* **2024**, *36*, 2310143.

[49] C. Ye, Y. Jiao, H. Jin, A. D. Slattery, K. Davey, H. Wang, S. Z. Qiao, *Angew. Chem., Int. Ed.* **2018**, *57*, 16703.

[50] Y. Wang, R. Zhang, J. Chen, H. Wu, S. Lu, K. Wang, H. Li, C. J. Harris, K. Xi, R. V. Kumar, S. Ding, *Adv. Energy Mater.* **2019**, *9*, 1900953.

[51] L. Ni, J. Gu, X. Jiang, H. Xu, Z. Wu, Y. Wu, Y. Liu, J. Xie, Y. Wei, G. Diao, *Angew. Chem., Int. Ed.* **2023**, *62*, 202306528.

[52] H. Li, M. Chuai, X. Xiao, Y. Jia, B. Chen, C. Li, Z. Piao, Z. Lao, M. Zhang, R. Gao, B. Zhang, Z. Han, J. Yang, G. Zhou, *J. Am. Chem. Soc.* **2023**, *145*, 22516.

[53] X. Li, Q. Guan, Z. Zhuang, Y. Zhang, Y. Lin, J. Wang, C. Shen, H. Lin, Y. Wang, L. Zhan, L. Ling, *ACS Nano* **2023**, *17*, 1653.

[54] Y. Xu, W. Yuan, C. Geng, Z. Hu, Q. Li, Y. Zhao, X. Zhang, Z. Zhou, C. Yang, Q. Yang, *Adv. Sci.* **2024**, *11*, 2402497.

[55] Z. Wang, H. Zhu, J. Jiang, H. Dong, F. Meng, J. Ke, H. Ji, L. Xu, G. Li, Y. Fu, Q.i Liu, Z. Xue, Q. Ji, J. Zhu, S. Lan, *Angew. Chem., Int. Ed.* **2024**, *63*, 202410823.

[56] Z. Li, Y. X. Yao, S. Sun, C. B. Jin, N. Yao, C. Yan, Q. Zhang, *Angew. Chem., Int. Ed.* **2023**, *62*, 202303888.

[57] Q. Gu, Y. Cao, J. Chen, Y. Qi, Z. Zhai, M. Lu, N. Huang, B. Zhang, *Nano-Micro Lett.* **2024**, *16*, 266.

[58] Z. Chen, M. Lu, Y. Qian, Y. Yang, J. Liu, Z. Lin, D. Yang, J. Lu, X. Qiu, *Adv. Energy Mater.* **2023**, *13*, 2300092.

[59] J. Zhou, C. Zhang, C. Xie, H. Wang, H. Fan, Y. Guo, C. Wang, F. Chen, Y. Ding, Q. Huang, Z. Zheng, *Adv. Energy Mater.* **2024**, *14*, 2303063.

[60] Z. Huang, Y. Zhu, Y. Kong, Z. Wang, K. He, J. Qin, Q. Zhang, C. Su, Y. L. Zhong, H. Chen, *Adv. Funct. Mater.* **2023**, *33*, 2303422.

[61] T. Lai, A. Manthiram, *Adv. Funct. Mater.* **2024**, *34*, 2405814.

[62] Y. Chen, X. Zhang, Q. Chen, D. Cai, C. Zhang, B. Sa, H. Zhan, *Adv. Funct. Mater.* **2025**, *35*, 2411941.

[63] Y. Lin, J. Wang, X. Zhang, X. Cheng, Q. Zhuang, J. Zhang, Q. Guan, Y. Wang, C. Shen, H. Lin, L. Zhan, L. Ling, Y. Zhang, *Adv. Funct. Mater.* **2025**, *35*, 2501496.

[64] F. Na, X. Li, J. Wang, X. Cheng, J. Zhang, Y. Wang, H. Lin, L. Zhan, L. Ling, Y. Zhang, *Energy Storage Mater.* **2025**, *78*, 104228.

[65] K. Chen, A. Hu, G. Zhu, Y. Li, J. Jiang, B. Yang, T. Li, K. Li, J. Chen, W. Xu, Z. Wang, R. Xu, W. Yang, J. Wang, G. Wu, J. Long, Z. Seh, *ACS Nano* **2025**, *19*, 14284.

[66] R. Xu, A. Hu, Z. Wang, K. Chen, J. Chen, W. Xu, G. Wu, F. Li, J. Wang, J. Long, *J. Energy Chem.* **2025**, *105*, 35.

[67] Z. Wang, C. Su, R. Xu, K. Li, B. Yang, T. Li, K. Chen, W. Xu, J. Chen, F. Li, B. Li, A. Hu, J. Long, *Energy Storage Mater.* **2025**, *75*, 104105.

2508225 (11 of 11)